Stable Wettability Control of Nanoporous Microstructures by iCVD Coating of Carbon Nanotubes

Hossein Sojoudi,[†] Sanha Kim,[‡] Hangbo Zhao,[‡] Rama Kishore Annavarapu,[†] Dhanushkodi Mariappan,[‡] A. John Hart,[‡] Gareth H. McKinley,*[,‡] and Karen K. Gleason*[,§]

[†]Department of Mechanical, Industrial and Manufacturing Engineering (MIME), The University of Toledo, 4006 Nitschke Hall, Toledo, Ohio 43606, United States

[‡]Department of Mechanical Engineering, Massachusetts Institute of Technology, 77 Massachusetts Avenue, Cambridge, Massachusetts 02139, United States

[§]Department of Chemical Engineering, Massachusetts Institute of Technology, 77 Massachusetts Avenue, Cambridge, Massachusetts 02139, United States

Supporting Information

ABSTRACT: Scalable manufacturing of structured materials with engineered nanoporosity is critical for applications in energy storage devices (i.e., batteries and supercapacitors) and in the wettability control of surfaces (i.e., superhydrophobic and superomniphobic surfaces). Patterns formed in arrays of vertically aligned carbon nanotubes (VA-CNTs) have been extensively studied for these applications. However, the as-deposited features are often undesirably altered upon liquid infiltration and evaporation because of capillarity-driven aggregation of low density CNT forests. Here, it is shown that an ultrathin, conformal, and low-surface-energy layer of poly perfluorodecyl acrylate, poly($1H,1H,2H,2H$-perfluorodecyl acrylate) (pPFDA), makes the VA-CNTs robust against surface-tension-driven aggregation and densification. This single vapor-deposition step allows the fidelity of the as-deposited VA-CNT patterns to be retained during wet processing, such as inking, and subsequent drying. It is demonstrated how to establish omniphobicity or liquid infiltration by controlling the surface morphology. Retaining a crust of entangled CNTs and pPFDA aggregates on top of the patterned VA-CNTs produces micropillars with re-entrant features that prevent the infiltration of low-surface-tension liquids and thus gives rise to stable omniphobicity. Plasma treatments before and after polymer deposition remove the crust of entangled CNTs and pPFDA aggregates and attach hydroxyl groups to the CNT tips, enabling liquid infiltration yet preventing densification of the highly porous CNTs. The latter observation demonstrates the protective character of the pPFDA coating with the potential application of these surfaces for direct contact printing of microelectronic features.

KEYWORDS: pPFDA coating, CNT micropillars, elastocapillary densification, superhydrophobicity, omniphobicity, wettability control
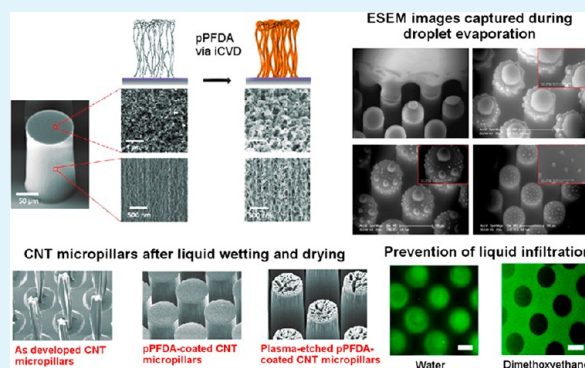
INTRODUCTION

Chemical-vapor-deposition (CVD) synthesis of vertically aligned carbon nanotubes (VA-CNTs)[1] using lithographically patterned catalyst films[2−4] directly creates bulk microstructures, which have tunable electrical and mechanical properties[5] as well as high porosity (>99%)[6−8] and whose large surface area is favorable for charge transport[9] and electrochemical interactions.[7,10] The mutual control of microscale geometry and nanoscale porosity is attractive for battery[10] and supercapacitor electrodes,[9,11] surfaces with controlled wettability,[12] and direct contact printing of liquid inks.[13] However, the large surface area and porous structure of VA-CNT arrays make them highly susceptible to surface forces, such as the liquid capillary force. Chandra et al. have shown that the mechanical compliance and the large surface area of polymer micropillars also make these structures susceptible to deformation and top-gathering

(aggregation) because of adhesive and capillary surface forces.[14] As liquid evaporates off the micropillar arrays, the individual pillars bend and aggregate together ("top-gather") because capillary−meniscus-interaction forces are greater than elastic-restoring forces, whereas the micropillar structures are surrounded by a continuous liquid body.[14] This process, also referred to as elastocapillary coalescence, aggregation, or self-assembly, has also been described for the well-known phenomena of clumping in wet hair[15] or in a paintbrush immersed in paint.[16] For porous micropillar arrays, such as VA-CNTs, the process of elastocapillary aggregation can be accompanied by densification in the nano and micro filaments,

also referred to as elastocapillary densification (shrinkage). This process has been used as a fabrication step to enhance the functionality of carbon nanotubes (CNTs) for applications in microelectronics, interconnects, MEMS devices, micro sensors, trapping devices, bioprobes, and energy storage devices.[17] De Volder et al. have demonstrated an enhancement in the mechanical robustness of the CNTs through capillary densification (100-fold enhancement in the Young's modulus) and have developed 3D microstructures as molds for the mass production of 3D polymer structures.[18] In another study, they have shown a decrease of more than 3 orders of magnitude in the contact resistance of the CNT electrodes after elastocapillary densification.[19]

Various methods of exposure to liquids, such as immersion, directed immersion, dipping, and condensation, have been employed to obtain complex and hierarchical features via capillary self-assembly of nanoscale filaments.[17,18,20] In addition, the shape and periodicity of the self-assembled microstructures can be tuned by changing the aspect ratio, spacing, tilt, and elastic modulus of the CNT micropillars.[21] These processes have been comprehensively studied and optimized to achieve uniform results over larger areas and to adapt the processes to structures with different dimensions and spacing. The hierarchical structures that are formed after liquid exposure and drying have been classified as top-gathering, winding, folding, or foaming, depending on the liquid exposure method and the number of pillars.[17] Lithographically patterned CNT pillars primarily experience densification through condensation of the liquid or dipping in the liquid and subsequent drying. Here, we clarify that we refer to elastocapillary aggregation (top-gathering) only when the micropillars top-gather and to elastocapillary densification only when the individual micropillars, each composed of a vertically aligned forest of CNTs, shrink radially. Despite these advances, elastocapillary top-gathering and densification due to surface-tension forces exerted during liquid infiltration and evaporation[17] have prevented development of applications that leverage the porosity of the CNT forest within a liquid environment.

Here, we show that the elastocapillary densification and top-gathering of the porous CNT microstructures are prevented by conformal deposition of an ultrathin, low-surface-energy, and protective layer of poly perfluorodecyl acrylate, poly-(1H,1H,2H,2H-perfluorodecyl acrylate) (pPFDA) on the CNTs via initiated chemical vapor deposition (iCVD). iCVD is a solventless, free-radical, polymerization mechanism that enables conformal and ultrathin deposition of polymers onto porous and large-surface-area substrates at low temperatures, preserving the functionality of monomers.[22−25] Polymer deposition on CNTs has been studied to improve functionality of CNT-based devices and products. Rivadulla et al. have studied layer-by-layer deposition of polymers on a random network of CNTs to tune their electrical and thermal properties.[26] He et al. have deposited uniformly thin carbon−fluorine films on the surfaces of aligned carbon nanotubes by means of a plasma-polymerization treatment.[27] Polymer coating via the vapor-based and solvent-less iCVD method has also been studied to form polymeric duplicates of rose-petal structures.[28] Lau et al. favored a bioinspired approach to the problem of developing superhydrophobic surfaces, using iCVD to help mimic designs found in nature.[12] They enhanced the superhydrophobic effect on CNTs by combining two elements: the coating of VA-CNTs with hydrophobic poly-(tetrafluoroethylene) (PTFE) and the nanoscale roughness inherent in the sample. Ye et al. have demonstrated a successful transfer of aligned, multiwalled carbon nanotubes (MWNTs) after functionalizing them with poly(glycidyl methacrylate) (PGMA) via iCVD.[29] They have also shown improved mechanical properties and stability in MWNTs after polymer deposition. In addition, PTFE,[12] Gold−Thiol,[30] and parylene coatings[31] on CNTs have been studied. However, these studies have only focused on the interaction of aqueous droplets with these surfaces; a comprehensive study of liquid-wetting and evaporation mechanisms for liquids with a range of surface tensions has not been performed, and studies have not provided controllable methods for liquid infiltration and evaporation without aggregation of the porous CNT forests.

Here, we show how to fabricate liquid-stable nanoporous-CNT microstructure arrays, whose wettability can also be controlled. We utilize in situ microscopy and imaging to examine the liquid-infiltration and drying processes in the CNT microstructures. The crust of entangled CNTs on top of the forests and micropillars, formed during the synthesis of the VA-CNTs,[32] gives rise to the presence of surface sites where polymer condensation with subsequent cluster formation can occur during the iCVD polymerization process. Two scenarios are studied by controlling surface energy and morphology. In the first scenario, the crust of entangled CNTs on top of the forests and micropillars, which is coated with the pPFDA aggregates, forms a nanotextured surface possessing re-entrant features that prevent the infiltration of low-surface-tension liquids (i.e., hexadecanethiol, dimethoxyethane, acetone, and ethylene glycol), resulting in omniphobicity. Confocal microscopy verifies the prevention of liquid infiltration into these pPFDA-coated CNT micropillars. In addition, the pPFDA coating strengthens the individual nanotubes in the VA-CNT micropillars and prevents the onset of elastocapillary top-gathering. An increase in the compression-elastic modulus of the VA-CNT micropillars from 24 to 28 MPa is observed as a result of pPFDA coating.[33] In the second scenario, oxygen-plasma treatments are employed before and after the pPFDA deposition to remove the crust of entangled CNTs and the pPFDA aggregates deposited on top of the micropillars, enabling axial infiltration of wetting liquids into the micropillars. The mechanical reinforcement provided to the CNT-CNT junctions by iCVD polymer deposition stabilizes the CNT forest within the micropillars against elastocapillary densification, during the process of liquid infiltration and subsequent evaporation. Scanning electron micrographs (SEMs), obtained after both the wetting of the pPFDA-coated CNT micropillars with a probe liquid seeded with silver nanoparticles and subsequent drying, verify the infiltration of the liquid without densification (shrinkage) of the CNTs. In a separate study, we discuss the application of the porous pPFDA-CNT-composite microstructures as printing stamps in the fabrication of electronic features.[33] This work demonstrates the robust retention of VA-CNT patterns with tunable geometry, mechanical characteristics, wettability, and surface properties and thus opens up new avenues for applications of patterned CNT forests that utilize wet processing environments.

■ RESULTS AND DISCUSSION

Vertically aligned carbon nanotubes (VA-CNTs) are synthesized on silicon substrates, which are coated with multilayered catalyst films, via chemical vapor deposition (CVD). Patterning of the catalyst layers by photolithography enables fabrication of
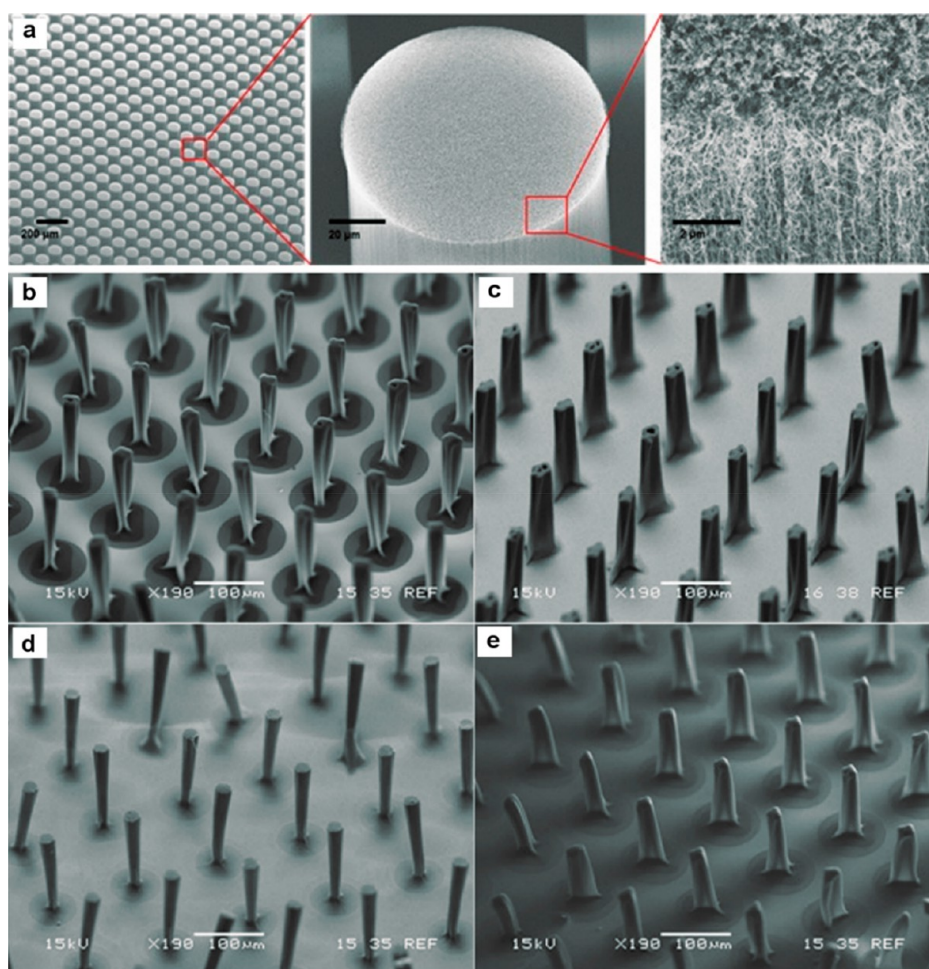
Figure 1. SEM micrographs of micropillars formed from VA-CNTs with a ~120 μm height (h), ~50 μm radius (r), and ~130 μm center-to-center spacing (d) imaged (a) as deposited or after wetting and subsequent drying with (b) dimethoxyethane (γ_D = 20.4 ± 0.7 mN/m), (c) water (γ_W = 71.5 ± 0.9 mN/m), (d) hexadecanethiol (γ_H = 28.2 ± 1.6 mN/m), or (e) acetone (γ_A = 25.8 ± 1.3 mN/m). Capillarity-driven densification in the CNT micropillars is seen in (b), (c), (d), and (e), and the specific features of the axial shrinkage of each pillar is observed to vary with the thermophysical properties of the wetting liquid, such as the surface tension, viscosity, and evaporation rate.

VA-CNT features with the desirable cross-sectional shapes. Figure 1a shows SEM images of patterned VA-CNT micropillars (hereafter denoted as CNT micropillars). The height (h), radius (r), and center-to-center spacing (d) of the CNT micropillars are ~120, ~50, and ~130 μm, respectively. CNT micropillars are exposed to different liquids (water, hexadecanethiol, dimethoxyethane, and acetone) by directly flooding the substrate with approximately 100 μL of the each liquid. Videos S1 and S2 show side views of the CNT micropillars during wetting and drying with dimethoxyethane and hexadecanethiol, respectively. We ensure that the liquids spread over the samples; reach the silicon substrate, on which the CNT micropillars are synthesized; and wet the CNT micropillars from the base (capillary wetting). Next, the liquids are evaporated in ambient conditions from the substrate and from the perimeter of the CNT micropillars, as the curved meniscus between the individual pillars recedes. Finally, the liquids evaporate from within each of the porous CNT micropillars, often causing the micropillars to shrink (densify) as this stage of the evaporation proceeds (elastocapillary densification or shrinkage). In situ optical imaging identifies the sequential stages of liquid infiltration, evaporation, and densification; the kinetics related to the size and shape of the

CNT micropillars; and the thermophysical properties of the wetting liquids (Figure S8).

The mechanism of elastocapillary densification is based on a competition between elastic and surface-tension forces. It has been shown that when the forces exerted by the liquid exceed the elastic-restoring forces of the individual CNT filaments, the CNTs densify into solid aggregates as the infiltrated liquid evaporates over the time.[17] Here, densification is observed mostly during liquid drying, which is in accord with previous reports.[11] The lack of elastocapillary top-gathering in the CNT micropillars, observed during evaporation of the liquids as the meniscus recedes, is due to the relatively large spacing between individual CNT micropillars and their relatively low aspect ratio. It is evident from the videos (see Supporting Information) that the CNT micropillars constrain the liquid during the final stage of liquid evaporation and densification in the CNTs. During the evaporation of the liquid from the pillars, the liquid is pinned to the outer surface of the pillars, and evaporation causes densification as the liquid–air and solid–air interfaces coincide.[34] Figure 1b–e shows SEM images of the final shapes of the densified CNT micropillars, after having been wetted with dimethoxyethane, water, hexadecanethiol, or acetone, respectively, and allowed to dry. We chose these liquids on the basis of the interest in preventing aggregation in
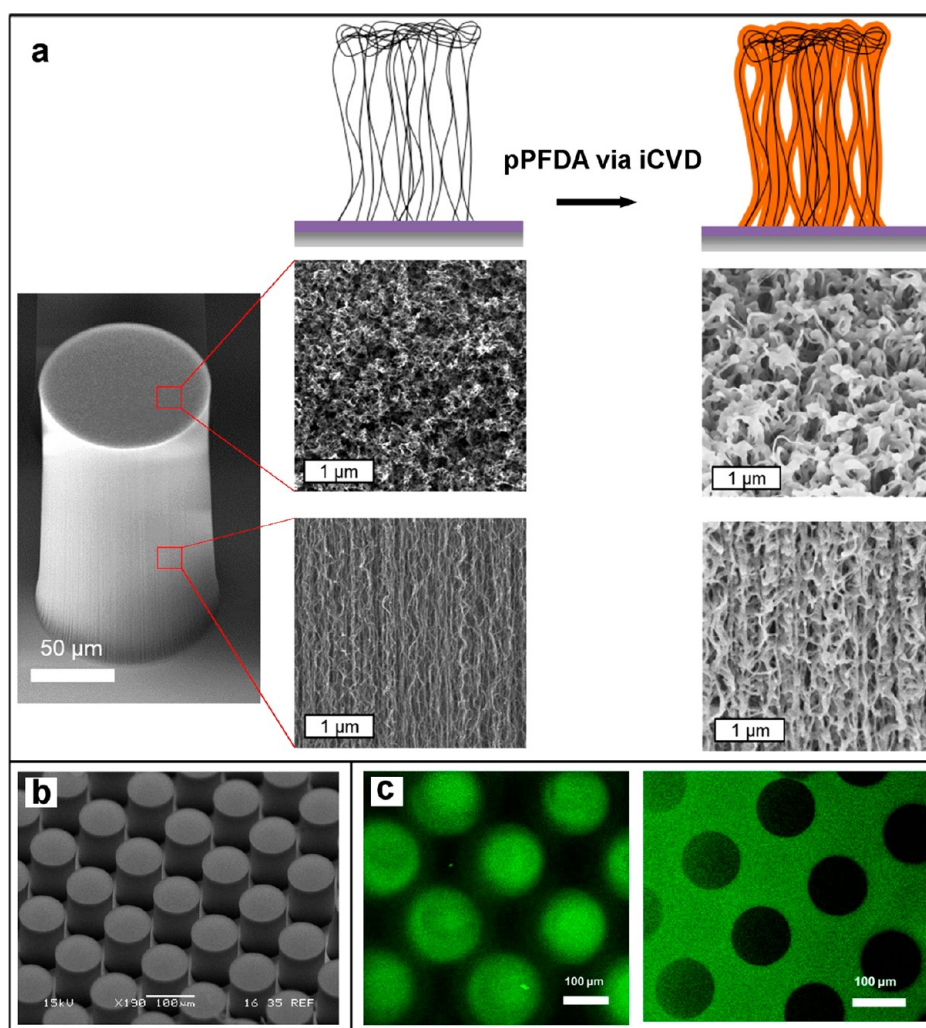
Figure 2. Preventing densification and elastocapillary self-assembly formation by iCVD deposition of pPFDA. (a) Schematic of pPFDA deposition (top panel), SEM image of a single CNT micropillar (left panel), and top-view and side-view SEM images of unmodified (middle panel) and pPFDA-coated (right panel) CNT micropillars. (b) SEM image of pPFDA-coated CNT micropillars after wetting with hexadecanethiol and subsequent drying. No densification is observed, indicative of the protective nature of the pPFDA coating. (c) Confocal-microscopy images captured during the drying process after the wetting of the unmodified CNT micropillars with water (middle panel) or pPFDA coated CNT micropillars with dimethoxyethane (right panel). Presence of green-dyed water within the pillars in the unmodified sample (middle panel) and absence of the green-dyed dimethoxyethane in the pPFDA-coated sample (right panel) indicate that water infiltrates into the pillars in the unmodified sample, but even a low-surface-tension liquid like dimethoxyethane (which has very low surface tension when compared to water) only wets the interpillar area in the coated sample. The scale bar in (c) is 100 μm.

carbon nanotubes used in applications that involve interaction with these liquids. Dimethoxyethane is a clear, colorless, aprotic, liquid ether that is used as a solvent, especially in batteries;[10] hexadecanethiol is frequently used as a molecular ink in microcontact printing using self-assembled monolayers;[13] water and acetone are two of the most frequently used solvents. Depending on the wetting method (dipping, immersion, or condensation), the geometry of the pillars, their aspect ratios (both in-plane and out-of-plane), the thermophysical properties of the wetting liquid (e.g., surface tension, viscosity, and evaporation rate), and the presence of any external constraints, various hierarchical features can be obtained.[17] We measured the surface tensions of dimethoxyethane ($\gamma_D = 20.4 \pm 0.7$ mN/m), water ($\gamma_W = 71.5 \pm 0.9$ mN/m), hexadecanethiol ($\gamma_H = 28.2 \pm 1.6$ mN/m), and acetone ($\gamma_A = 25.8 \pm 1.3$ mN/m) using the pendant-drop method. Here, the different elastocapillary-induced hierarchical features observed in the CNT

micropillars is mainly due to the influence of the different surface tensions of the liquids (see Figure 1).

To control the wettability of the CNT micropillars and to enhance their mechanical properties when exposed to liquids, a secondary coating with controlled conformity, surface chemistry, and topography is needed. To this end, we deposit an ultrathin layer of poly perfluorodecyl acrylate, poly-(1H,1H,2H,2H-perfluorodecyl acrylate) (pPFDA), on the CNT micropillars via initiated chemical vapor deposition (iCVD) and study the impact of this protective layer on the wettability of the micropillars. In the iCVD process (Figure S1), initiator molecules, *tert*-butyl peroxide (TBPO), thermally break down into radicals (−TBO) by filament heating ($T_f = 250$ °C). The initiator free radicals (−TBO) attack the PFDA monomer to create monomer PFDA radicals. The monomer PFDA radical adds to another PFDA monomer during propagation or reacts with another monomer radical during termination. As the molecular weight grows, the pPFDA

polymers then adsorb on the surface of the substrate (CNT sample or control Si), which is maintained at a low temperature (T_s = 30 °C). The deposition thickness can be monitored in situ via laser interferometry and the deposition uniformity along the CNT sidewalls can be controlled via the exposure time and deposition rate. iCVD coating of poly(methacrylate acid) (PMAA) has been applied to elastomeric poly-(dimethylsiloxane) (PDMS) pillars to form stable clusters by the wetting of the micropillars with solvents and subsequent evaporation. When the solvent softens and mobilizes polymer chains and enables them to interdiffuse, visible polymer welds connect the edges of adjacent CNTs as bonds occur.[35]

It has been shown that the pillars can be fully and controllably restored to their upright position after complete evaporation of the solvent, resulting in potential application of these surfaces in drug delivery.[36] For the same application, Aizenberg and co-workers have also studied the stability and reversibility of micro clusters produced by evaporation-induced assembly of micropillars.[37] Here, we intentionally deposited a low-surface-energy and ultrathin polymer film (between 5 and 30 nm thick) to control wettability of the CNT micropillars and improve their mechanical properties when exposed to a variety of liquids. Figure 2a shows a schematic of pPFDA deposition, an SEM image of a CNT micropillar, and zoomed top-view and side-view SEM images before and after pPFDA deposition (30 nm thick). Comparison of the SEM images before and after pPFDA deposition clearly shows the presence of polymer on the sides and on the tops of the CNTs in addition to thickening of the individual CNTs.

Energy-dispersive X-ray spectroscopy (EDX) is also performed to verify the coating uniformity of the CNT pillars with the fluorine-rich pPFDA (Figure S2). EDX mapping shows the presence of fluorine only on the pPFDA-coated micropillars and that it is uniformly distributed on the pillars. We hypothesize that during iCVD polymerization, the monomer vapor and free radicals are able to diffuse into the densely packed nanotube forests and result in conformal deposition of an ultrathin, solid polymer film on the individual nanotube sidewalls. EDX spectra randomly collected at multiple spots of the unmodified and the pPFDA-coated CNT micropillars indicate the presence of detectable fluorine peaks only from the coated samples.

To further confirm the presence of functional groups, Fourier-transform infrared spectroscopy (FTIR) and X-ray photoelectron spectroscopy (XPS) were also performed on a 30 nm thick pPFDA film deposited on a smooth silicon (Si) substrate as a control sample. The sharp peak at 1741 cm^{-1} in the FTIR spectrum is caused by $-C=O$ stretching (Figure S3). The peaks at 1246 and 1207 cm^{-1} are caused by asymmetric stretching and symmetric stretching of the $-CF_2-$ moiety. The sharp peak at 1153 cm^{-1} is caused by the $-CF_2-CF_3$ end group, confirming that the pPFDA coating retains the CF_2 and CF_3 moieties originating from the pendant functional group of the monomer. The XPS spectra show C1s, O1s, and F1s as the most prominent peaks (Figure S4). The F1s peak at 688.4 eV confirms the presence of the fluorine groups (Figure S4b). The five C1s peaks in the XPS spectrum in Figure S4c are due to five bonding environments (C1: $-C^*F_3$, C2: $-C^*F_2$, C3: $-C^*=O$, C4: $-O-C^*H_2-CH_2-$, and C5: $-C-C^*H_2-C-$), as expected for vinyl polymerization of the PFDA monomer.

The morphology of the pPFDA-coated CNTs depends on the pPFDA deposition rate and the nature of the crust of entangled CNTs. The pPFDA conformal coating initially wraps around the individual CNTs, resulting in a decrease in the penetration depth of the pPFDA coating into the CNT forests from the tops and the side walls. Aggregates of pPFDA coated on the crust of entangled CNTs (which we refer to as re-entrant features)[38] form on the top, whereas bundling of CNTs happens on the side walls of the micropillars. The size and shape of the re-entrant features depend on the pPFDA-deposition time and thickness and also on the form of the crust of entangled CNTs. The bundling at the side wall is due to growth of the pPFDA thickness until it spans between adjacent CNTs. Additional SEM images acquired on the top, side, and bottom of a pPFDA-coated CNT pillar show that the pPFDA coating wraps around each nanotube without altering the structure or orientation of the CNTs (Figure S5).

The pPFDA-coated CNT micropillars are wetted with liquids and dried in a similar manner to the unmodified CNT micropillars. Videos S3 and S4 show wetting of the pPFDA-coated CNT micropillars with water and hexadecanethiol and their subsequent drying. Unlike the unmodified micropillars, no densification (shrinkage) is observed for the pPFDA-coated micropillars, indicating the protective nature of the pPFDA layer. Figure 2b shows an SEM image of a pPFDA-coated CNT micropillars array after wetting with hexadecanethiol and subsequent drying. Because of the liquid-repelling nature of the coated pillars, the coated arrays were confined in a small container in order to prevent sessile droplets from rolling off the samples and to facilitate their wetting process. It is clear from the SEM images acquired from the tops of the pillars that a crust of entangled CNTs is present on the tops of the pillars (Figure 2a, middle panel). These crusts provide surface sites for the pPFDA polymer to further condense on the tops of the pillars during iCVD polymerization (Figures S5 and S6). This gives rise to an enhanced presence of hierarchical features on the tops of the micropillars, on a length scale smaller than the length of the VA-CNTs, which provides unique, enhanced antiwetting properties. In addition, the constraints both at the top and on the bottom of the CNT pillars (the crust of entangled CNTs coated with pPFDA aggregates) give rise to axial anisotropy in the mechanical properties of the CNTs, which plays an important role in the prevention of elastocapillary aggregation. We hypothesize that the low-surface-energy polymer coating (pPFDA) sheathed around the VA-CNTs prevents infiltration of low-surface-tension liquids into the forests within the pillars. However, it is evident from the in situ videos captured during wetting and drying that the liquids enter the interstitial spaces between the CNT micropillars. To further verify this, we employed in situ confocal-microscopy imaging during the wetting and drying processes. A fluorescent dye (Fluorescein sodium salt, F6377 Sigma-Aldrich) is mixed with the wetting liquid (water or dimethoxyethane). The imbibition and subsequent evaporative drying of the dilute solution (1 wt %) are imaged by confocal microscopy. Figure 2c shows confocal-microscopy images focused near the bottom of the CNT micropillars during drying. The middle panel reveals the infiltration of the green-dyed water into unmodified micropillars. The right panel shows that the interior of the pPFDA-coated micropillars resists infiltration of the dyed dimethoxyethane. The dimethoxyethane, having a much lower surface tension than water, wets only the interpillar area in the pPFDA-coated sample. Further 3D confocal images at different axial positions confirmed the presence of water within the entire columnar region of the micropillars in the unmodified sample and presence of
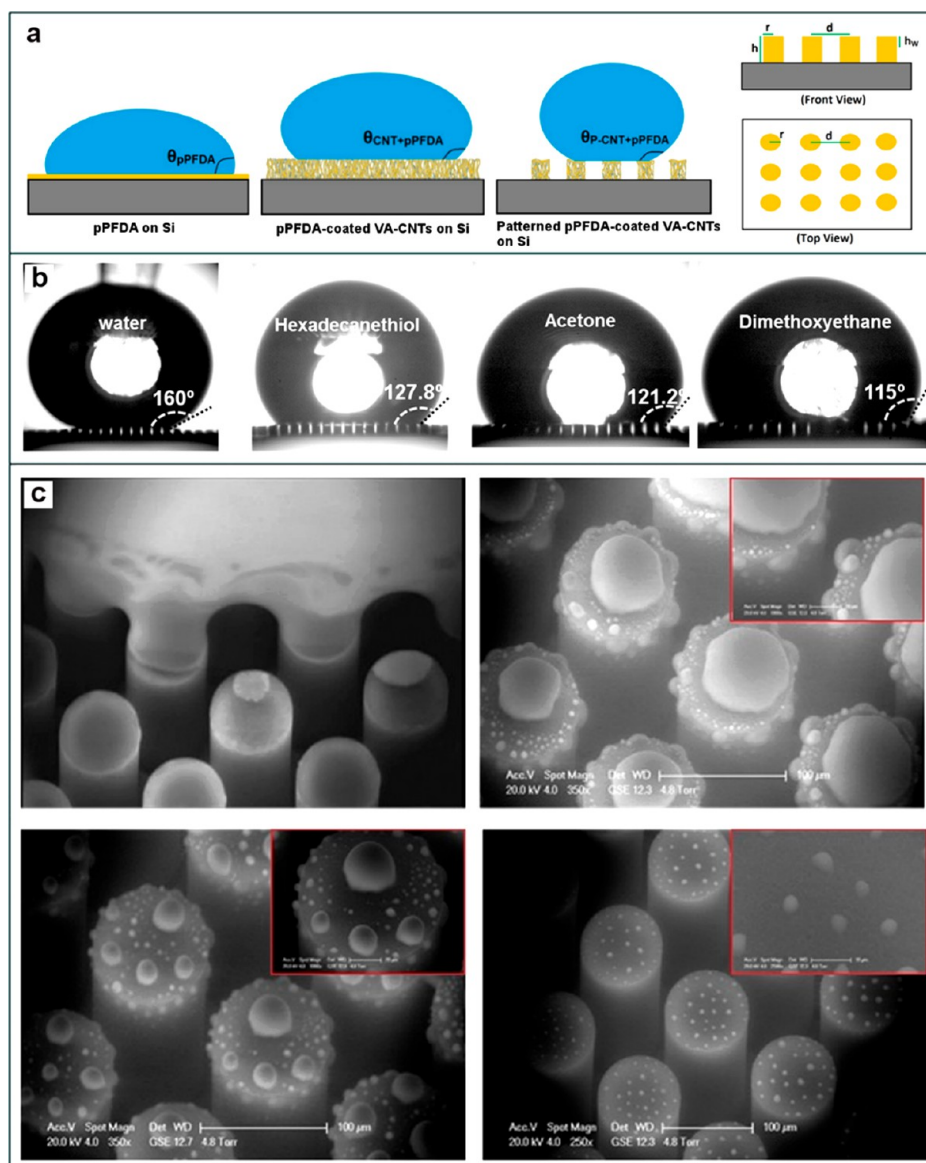
Figure 3. (a) Schematic of a droplet on a relatively smooth pPFDA surface, on a pPFDA-coated VA-CNT forest, and on pPFDA-coated VA-CNT micropillars and a schematic showing the geometry of the pillars (radius, r = 50 μm; height, h = 120 μm; center-to-center spacing, d = 130 μm; and side-wall wetting, h_w). (b) Images of approximately 5 μL droplets of water, hexadecanethiol, acetone, and dimethoxyethane, captured during contact-angle measurements, show the presence of air pockets between the droplet base and the coated CNT micropillars, indicating a Cassie−Baxter wetting state and omniphobicity. (c) Sequential environmental SEM images captured during the drying of a single hexadecanethiol droplet on an array of pPFDA-coated CNT pillars indicate the formation of capillary bridging. Insets in (c) show zoomed ESEM images.

dimethoxyethane only in the interpillar area in the pPFDA-coated sample during the drying step (Figure S7a,b). Both the unmodified and pPFDA-coated pillars remain cylindrical and undistorted during the liquid drying step. Upon drying, the meniscus recedes and exerts capillary forces on the micropillars; however, these forces are not strong enough to overcome the elastic strength of the reinforced CNTs and cause no top-gathering in the structure of the micropillars. Similarly, confocal micrographs demonstrate that the pPFDA-coated CNT micropillars resist the infiltration of dyed water and dimethoxy-ethane (Figure S7c,d). The confocal images of the unmodified samples, immediately after flooding with the dyed liquids, look entirely green. Therefore, images are recorded after partial liquid evaporation when the micropillars become visible under the microscope. Videos S5−S8 show sequential snapshots of confocal-microscopy images captured during evaporation of

green-dyed water and dimethoxyethane from both unmodified and pPFDA-coated CNT micropillars.

Additional confocal-microscopy images focused on the tops of the unmodified CNT micropillars are obtained as the green-dyed water within the pillars evaporates. Due to the wide disparity in length scales that control the meniscus curvature, water initially evaporates from the interpillar area and then at later times evaporates from within the individual pillars. Snapshot images show that the cross-sectional area of the top of each micropillar decreases as the fluorescent-dyed water evaporates (Figure S8). This decrease is consistent with the densification (shrinkage) observed in the SEM images of the unmodified samples after water imbibition and evaporation (Figure 1c). The change in dimensions of the micropillars after wetting and drying represents an undesirable loss in pattern fidelity as a result of wet processing.

Table 1. Surface-Tension and Contact-Angle (CA) Values Measured by Goniometry[a]

	water	hexadecanethiol	acetone	dimethoxyethane
surface tension, γ (mN/m)	71.5 ± 0.9	28.2 ± 1.6	25.8 ± 1.3	20.4 ± 0.7
CA on pPFDA/Si, θ_{pPFDA} (°)	119.0 ± 1.0	68.5 ± 2.4	65.3 ± 2.8	61 ± 1.5
CA on CNT forest, θ_{CNT} (°)	128.4 ± 2.7	0[b]	0[b]	0[b]
CA on CNT micropillars, $\theta_{P\text{-}CNT}$ (°)	133.5 ± 1.9	0[b]	0[b]	0[b]
CA on pPFDA-coated CNT forest, $\theta_{CNT+pPFDA}$ (°)	151.0 ± 1.5	130.7 ± 1.9	125.0 ± 1.8	121 ± 2.5
CA on pPFDA-coated CNT micropillars, $\theta_{P\text{-}CNT+pPFDA}$ (°)	160.0 ± 1.8	127.8 ± 3.2	121.2 ± 1.4	115 ± 1.7
CA on pPFDA-coated CNT micropillars with plasma treatment, $\theta_{P\text{-}P\text{-}CNT+pPFDA}$ (°)	0[b]	0[b]	0[b]	0[b]

[a]CA values obtained from the goniometric measurements on the pPFDA-coated CNT forests and CNT micropillars indicate that the pPFDA polymer coating prevents infiltration of low-surface-tension liquids (including hexadecanethiol, acetone, and dimethoxyethane) into the CNTs. This is due to the presence of the crust of entangled CNTs, which is coated with aggregates of the pPFDA, creating surfaces that possess re-entrant features. [b]The liquid infiltrates.

Goniometric measurements of the water contact angle (WCA) are performed to evaluate the wettability of the unmodified and the pPFDA-coated CNT micropillars. Figure 3b shows representative droplet images captured during the WCA measurements. Hierarchical roughness with three length scales results from the combination of the micron-size patterns of CNT pillars, the mesoscale roughness of the top crust of entangled CNTs, and the intrinsic nanoscale roughness of the pPFDA. The pPFDA-coated micropillars are extremely superhydrophobic and exhibit a WCA ($\theta_{P\text{-}CNT+pPFDA}^{W}$) of 160 ± 1.8°, whereas a uniform VA-CNT forest (without micro patterns) presents a WCA ($\theta_{CNT+pPFDA}^{W}$) of 151 ± 1.5° because of the slightly higher wetted contact area. Water-droplet contact-angle values of 170° (mentioned as almost-spherical droplets in the journal), 163°, and 110° are reported on PTFE, gold–thiol, and parylene films, respectively. The contact angles on PTFE- and gold–thiol-coated CNT forests are higher than the contact angle observed on the pPFDA-coated CNT forest. The area fractions (f) were reported as 0.11 for PTFE-coated and 0.1 for gold–thiol-coated CNT forests and as 0.5 for parylene films. The calculated area fraction (f) of our pPFDA-coated CNT forest is 0.243, determined by using the Cassie–Baxter contact-angle equation. Because the contact angle of a water droplet on a smooth pPFDA-coated Si surface is measured as 119 ± 1° (the highest that can be obtained on a smooth surface), we believe that the higher contact angles on PTFE- and gold–thiol-coated CNT forests than on the pPFDA-coated CNT forests are due to the difference in the area fractions (f) between the samples. Our pPFDA-coated CNT forests have entangled crusts and pPFDA aggregates on the top, which increase the area fraction.

For a droplet on patterned pPFDA-coated CNT micropillars the presence of air pockets under the droplets suggests a Cassie–Baxter-like state.[21] A simplified form of the Cassie–Baxter equation yields the water-wet area of the pPFDA-coated CNT micropillars and pPFDA-coated, unpatterned VA-CNT forest, respectively. For a uniform forest of carbon nanotubes (as shown schematically in Figure 2a) we obtain

$$\cos \theta_{CNT+pPFDA}^{W} = f_{CNT+pPFDA}^{W} (1 + \cos \theta_{pPFDA}^{W}) - 1 \quad (1)$$

where $f_{CNT+pPFDA}^{W}$ is the water-wet fraction of the VA-CNT forest, and θ_{pPFDA}^{W} is the WCA on a flat pPFDA film deposited on a smooth silicon-wafer substrate and is measured to be $\theta_{pPFDA}^{W} = 119 ± 1°$. From eq 1, we determine the water-wet fraction of the VA-CNT forest to be $f_{CNT+pPFDA}^{W} = 0.243$, which gives us a rough estimate of the surface area on the tops of the pPFDA-coated CNTs (the crust of entangled CNTs top coated with the pPFDA). For a periodic array of micropillars,

rearranging the simplified Cassie–Baxter equation gives the water-wet area of the patterned CNT micropillars:

$$\cos \theta_{P\text{-}CNT+pPFDA}^{W} = f_{P\text{-}CNT+pPFDA}^{W} (1 + \cos \theta_{pPFDA}^{W}) - 1 \quad (2)$$

We obtain the water-wet area of the CNT micropillars $f_{P\text{-}CNT+pPFDA}^{W} = 0.117$ from eq 2, which, as expected, is lower than $f_{CNT+pPFDA}^{W}$ because of the presence of an interpillar area underneath the water droplet in the patterned CNT micropillars. If we assume that there is no side-wall wetting of the coated CNT micropillars by water, then we can calculate the water-wet fraction of the pillars, knowing the water-wet fraction of the VA-CNT forest ($f_{CNT+pPFDA}^{W} = 0.243$) and the cylindrical geometry of the pillars (see Figure 3a for details):

$$f_{P\text{-}CNT+pPFDA}^{C} = f_{pillar} \times f_{CNT+pPFDA}^{W} \quad (3)$$

where $f_{pillar} = \frac{A_{pillar}}{A_{total}} = \frac{\pi r^2}{d^2}$ and $r = 50$ μm and $d = 130$ μm are the radii and center-to-center spacings of the pillars, respectively. The calculated water-wet fraction of the micropillars is $f_{P\text{-}CNT+pPFDA}^{C} = 0.112$, which is lower than the water-wet fraction obtained directly from the goniometric measurements ($f_{P\text{-}CNT+pPFDA}^{W} = 0.117$), verifying that there is no side-wall wetting by the water droplets.

Goniometric measurements are repeated with droplets of the low-surface-tension liquids as hexadecanethiol ($\gamma_H = 28.2 ± 1.6$ mN/m), dimethoxyethane ($\gamma_D = 20.4 ± 0.7$ mN/m), and acetone ($\gamma_M = 25.8 ± 1.3$ mN/m). Table 1 summarizes the contact-angle values obtained from the goniometric measurements. Figure 3b shows representative droplet images of these low-surface-tension liquids on the coated CNT micropillars, illustrating the omniphobic character of these surfaces. The 3-fold multiscale coating and texture, which combines tuned roughness and a low-surface-energy conformal coating, result in formation of these omniphobic surfaces. In addition, during iCVD polymerization, the coating preferentially builds up on the tops of the pillars, where the crust of entangled CNTs are present, forming pPFDA aggregates and resulting in the formation of surfaces with slight re-entrant curvature. These features prevent infiltration of the low-surface-tension liquids into the micropillars, giving rise to omniphobicity.[38,39] Such re-entrant features are also essential to the performance of surfaces for applications in biomimetic actuators and smart adhesives as well.[38,40]

We reduced the thickness of the conformal pPFDA coating from 30 to 5 nm by changing the growth conditions and studied its impact on the wettability of the samples. Figure S9 shows the impact of the pPFDA-coating thickness, measured

on a smooth Si substrate during iCVD polymerization, on contact-angle values, measured on the pPFDA-coated CNT micropillars. A pPFDA deposition of 5 nm or more on Si ensures the presence of the pPFDA everywhere on the CNT samples, giving rise to high liquid-contact-angle values. Water, which has a high surface tension (71.5 ± 0.9 mN/m), reached a stable contact-angle value by a pPFDA coating of ∼5 nm thick, whereas dimethoxyethane, which has a surface tension of 20.4 ± 0.7 mN/m, reached a stable contact-angle value when the pPFDA coating was 30 nm thick. It is believed that a high pPFDA thickness results in the formation of larger re-entrant features, enabling nonwetting states to be established with liquids that have lower surface tension and giving rise to omniphobicity. To achieve constant omniphobicity with a wide range of liquids, we used a 30 nm thick pPFDA coating in this work.

We calculate the wetted fraction of the VA-CNTs with the low-surface-tension liquid dimethoxyethane using a modified Cassie−Baxter equation:

$$\cos\theta_{CNT+pPFDA}^D = f_{CNT+pPFDA}^D \times W_{CNT+pPFDA}$$
$$\times \cos\theta_{pPFDA}^D - (1 - f_{CNT+pPFDA}^D) \quad (4)$$

where $\theta_{CNT+pPFDA}^D = 121 \pm 2.5°$ is the droplet contact angle of dimethoxyethane on the VA-CNTs, $\theta_{pPFDA}^D = 61 \pm 1.5°$ is the dimethoxyethane-droplet contact angle on a smooth pPFDA surface, and $W_{CNT+pPFDA}$ is the Wenzel wetting roughness of the VA-CNTs. We can similarly write the modified Cassie−Baxter equation for the CNT micropillars as well:

$$\cos\theta_{P\text{-}CNT+pPFDA}^D = f_{pillar} \times f_{CNT+pPFDA}^D \times W_{P\text{-}CNT+pPFDA}$$
$$\times \cos\theta_{pPFDA}^D - [(1 - f_{CNT+pPFDA}^D)$$
$$\times f_{pillar} + (1 - f_{pillar})] \quad (5)$$

where $\theta_{P\text{-}CNT+pPFDA}^D = 115 \pm 1.7°$ is the dimethoxyethane-droplet contact angle on the CNT micropillars, and $W_{P\text{-}CNT+pPFDA}$ is the Wenzel wetting roughness of the CNT micropillars. The values of the Wenzel wetting roughness can be obtained from eqs 4 and 5: $W_{CNT+pPFDA} = 2.054$ and $W_{P\text{-}CNT+pPFDA} = 8.516$. We can relate the Wenzel wetting to the radii of the individual CNTs (r_{CNT}) and the side-wall wetting of the VA-CNTs ($h_{w,CNT+pPFDA}$) and CNT micropillars ($h_{w,P\text{-}CNT+pPFDA}$) using the following geometric relations:

$$W_{CNT+pPFDA} = \frac{\pi r_{CNT}^2 + 2\pi r_{CNT} \times h_{w,CNT+pPFDA}}{\pi r_{CNT}^2} \quad (6)$$

$$W_{P\text{-}CNT+pPFDA} = \frac{\pi r_{CNT}^2 + 2\pi r_{CNT} \times h_{w,P\text{-}CNT+pPFDA}}{\pi r_{CNT}^2} \quad (7)$$

If we assume that the radius of an individual CNT coated with the pPFDA is $r_{CNT} = 35$ nm (the radius of an individual unmodified CNT is approximately 5 nm) and that all of the CNTs are aligned vertically, we can obtain values for the side-wall wetting of the VA-CNTs and CNT micropillars (with a sessile droplet of dimethoxyethane) equal to $h_{w,CNT+pPFDA} = 18.4$ nm and $h_{w,P−CNT+pPFDA} = 187.9$ nm. These values indicate that even a low-surface-tension-liquid droplet remains on the tops of the pPFDA-coated CNTs with minimal side-wall wetting. Droplet images of these low-surface-tension liquids on the CNT micropillars confirm the presence of a Cassie−Baxter

state, with air pockets trapped between the micropillars and the low-surface-tension-liquid (Figure 3b).

We also studied the transition of a macroscopic droplet, originally resting on the surface in a Cassie−Baxter state, into microdroplets on the pPFDA-coated CNT micropillars by dynamic imaging using environmental scanning microscopy (ESEM), which allows control of the humidity and pressure inside the ESEM chamber. The dynamics of the contact-line motion are governed by surface heterogeneities that act as pinning sites to produce local deformations, leading to the adhesion and pinning of a macroscopic contact line.[41] Environmental SEM images captured during the drying of a hexadecanethiol macrodroplet on the pPFDA-coated pillars exhibit formation of capillary bridging (Figure 3c and Video S9). It has previously been shown that the adhesion of drops on superhydrophobic surfaces is governed by capillary bridges at the receding contact line.[41] Microcapillary bridges detach from the surface by necking and rupturing until a single microdroplet forms on top of each of the pillars. Further reductions in humidity result in recession of the contact line and formation of multiple microcapillary bridges, which detach from the surface by depinning and receding from each roughness feature. This results in the formation of microdroplets of 1−2 μm in size, which is on the same order of magnitude as the size of the bundles that are formed on top of the pillars from the crust of entangled CNTs coated with the pPFDA (Figure S6).

The results of the ESEM studies suggest that these microdroplets form and become preferentially stable on top of these bundles made from the crust of entangled CNTs coated with the pPFDA aggregates. We repeated the ESEM study with a droplet of a slightly higher surface-tension liquid (ethylene glycol, $\gamma_E = 48.8 \pm 1.0$ mN/m) of the same size. We observed similar microcapillary bridges (as observed for hexadecanethiol droplet), but in this case, the receding-liquid meniscus proceeds without the formation of microdroplets on top of the pPFDA-coated pillars (Figure 4 and Videos S10 and S11). We believe that this difference between hexadecanethiol and ethylene glycol evaporation is due to the lower molecular weight (62.068 g/mol) and hydrogen bonding of ethylene glycol, leading to a higher surface tension. The higher surface tension represents strong liquid bonding between molecules and a higher contact angle representing lower adhesion at the interface. The receding meniscus reaches the CNT micropillar edge without forming microdroplets, from which it detaches leaving a small portion of the droplet at the CNT micropillar edge.

The wettability of the CNT forest can be tuned by various surface treatments, such as oxygen-based functionalization by plasma,[42] selective decoration of the CNTs with nanoparticles,[43] and conformal-polymer deposition.[12] For example, plasma treatment can enable a tunable chemical modification of the CNT surface[44] through grafting of oxygen-containing groups onto the tips of the CNTs, thereby altering the polarity of the sample and leading to a more hydrophilic surface. Ramos et al. have shown that a CO_2-laser-irradiation post-treatment can reverse this hydrophilization.[45] It totally removes the grafted groups and re-establishes the hydrophobic character of the sample. They have reported the ability to control the wettability of CNTs (from superhydrophilicity to super-hydrophobicity) by combining both techniques.

Another important postgrowth treatment of the CNTs is the removal of the crust of entangled CNTs from the tops of the micropillars, which can be often observed on the as-grown
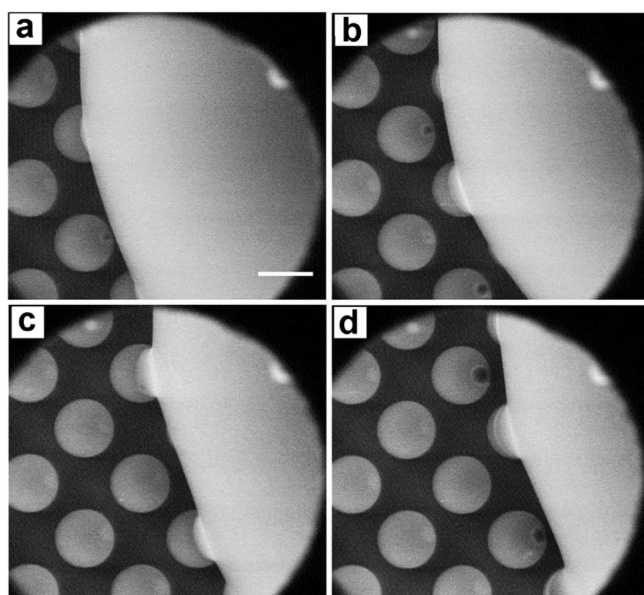
Figure 4. (a–d) Sequential ESEM images captured during evaporation of an ethylene glycol droplet (γ_{EG} = 47.7 ± 0.4 mN/m) on the pPFDA-coated CNT micropillars showing the formation of necks and the detachment of droplets from micropillars without rupture of the liquid or the formation of microdroplets on the top of each pillar (see Figure 3c). The scale bar is 100 μm.

CNTs.[46] Here, we apply oxygen-plasma treatments before and after polymer deposition to remove the crust of entangled

CNTs on the tops of the pillars as well as any pPFDA aggregates. Majumder et al. have also employed H_2O-plasma oxidation for excess removal of polymers and iron nanocrystals from the CNT tips.[47] We utilize the plasma treatment to study the impact of the pPFDA coating on the mechanical stability of the CNT structure when liquid infiltration is controlled. Figure 5a shows top-view SEM images acquired from the CNT pillars before and after each plasma treatment, indicating the successful removal of the crust of entangled CNTs and pPFDA aggregates from the tops of the pillars, which results in infiltration of liquids into the pPFDA-coated CNT pillars.

Figure S10 shows a schematic of plasma treatment and iCVD polymerization with some additional SEM images. Video S12 shows how a hexadecanethiol droplet infiltrates into the pillars immediately after being placed on the pPFDA-coated CNT micropillars. Oxygen-plasma etching has previously been shown to remove the entangled CNTs from the top of a CNT forest, resulting in liquid infiltration; however, significant densification along with radial contraction of the pillars is also observed.[19] Here, we allow liquid infiltration by plasma treatment but prevent densification via the conformal pPFDA sidewall coating of the individual CNTs. SEM images obtained after wetting and subsequent drying of the pPFDA-coated CNTs with a silver-containing liquid verify infiltration of the liquid without densification in the CNTs (Figure 5b).

It has been previously shown that the conformal coating of CNTs with Al_2O_3 using atomic layer deposition (ALD) decreases the extent of densification because of the anchoring of contacts between individual CNTs.[34] However, instead of densifying uniformly, the modified CNT microstructures
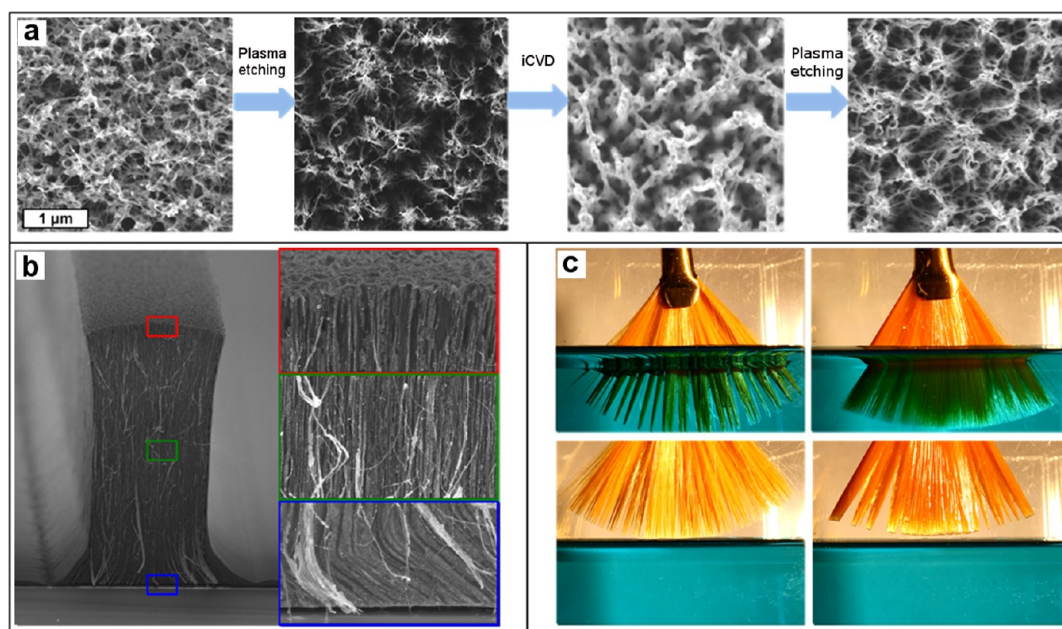
Figure 5. (a) SEM images acquired from the tops of the CNT micropillars before and after plasma treatment and iCVD polymerization. SEM images show that plasma treatment removes the crust of entangled CNTs as well as pPFDA aggregates from the tops of the pillars, resulting in liquid infiltration into the pillars. (b) SEM images of a cross section of plasma-treated pPFDA-coated CNTs after infiltration of a silver-containing liquid. SEM images show the presence of ink everywhere within the CNTs, confirming liquid infiltration; however, there is no densification due to the presence of the polymer coating. (c) Pictures of as-bought (right) and pPFDA-coated (left) paint brushes during immersion (top) and withdrawal (bottom) from blue-dyed water. A shiny appearance during the immersion of the coated brush (top left) suggests the partial presence of an insulating layer of air, called a plastron, trapped by the bristles of the brush. In the as-bought brush, there is no shiny appearance, and water fully wets the brush. During withdrawal of the as-bought brush from the water, a process of elastocapillary collapse (lateral shrinkage) takes place in the brush, influencing the orientation of its lamellae and forming bundles of lamellae (bottom right). By contrast, the pPFDA-coated brush comes out fully dry without any bundling or aggregation in its bristles (bottom left).

exhibit internal voids, which are similar to those observed during densification of short CNT forests or very low aspect-ratio CNT microstructures. An enhancement in the mechanical properties of the CNTs has also been observed after ALD coating, because the coating increases the density of the contact points, at which CNTs are rigidly held together and resist slipping relative to one another.[48] In addition, previous work with the ALD coating of Al_2O_3 has resulted in no change in the wettability of the CNT forest by the liquid (acetone). We have already discussed above that the intrinsically rough and low-surface-energy polymer coating (pPFDA) prevents the wettability of the surfaces even with low-surface-tension liquids (provided no plasma treatment is performed).

When liquid infiltrates into the CNT micropillars, the surface chemistry of the CNTs influences the strength of their interactions with liquids during wetting and drying. We hypothesize that a conformal coating of the individual CNTs with the pPFDA enhances the anchoring of the contacts between individual CNTs; reduces the inter-CNT pinning forces; and allows the stiff, elastic CNTs to recoil as the liquid evaporates.

Hierarchical bundling patterns can also be observed after immersion and withdrawal of a brush of parallel, elastic bristles into and out of a perfectly wetting liquid. Similar to the CNTs, the aggregation of bristles depends on a balance between the bristle elasticity and the capillary forces. To illustrate this principle, we immersed an as-bought paint brush and a pPFDA-coated brush into blue-dyed water to study the impact of surface coating on densification (shrinkage) and bundling (Videos S13–S14). A shiny appearance during the immersion of the coated brush suggests the partial presence of an insulating layer of air, called a plastron,[49] trapped by the brush bristles, indicating that the water does not fully come into contact with the bristles (Figure 5c). In the as-bought brush, there is no shiny appearance, and water fully wets the brush. During the withdrawal of the as-bought brush, a process of elasto-capillary collapse takes place in the brush, influencing the orientation of each bristle and forming bundles of bristles. This bundling process is associated with the capillary adhesion occurring during the withdrawal of the brush after liquid infiltration. The low-surface-energy pPFDA coating acts as nanoscale welds between the individual CNT contact points, establishing lateral interconnections and reinforcing elastic-restoring forces.

An analogy to this process can also be found in nature: namely, the tiny rows of hairs on the feet of geckos. Despite profound interest in the mechanics and performance of the gecko adhesive system,[50] relatively few studies have focused on their performance under conditions that are ecologically relevant to the natural habitats of geckos. Stark et al. have found that geckos can walk on wet surfaces, as long as their feet are reasonably dry. However, as soon as their feet get wet, they are barely able to hang to inclined surfaces such as walls and ceiling.[51] We believe that similar to the brush, wetting of the gecko's feet results in the bundling of the tiny hairs on its feet, negatively affecting their adhesive performance. It is also appropriate to note here the hydrophobic nature of the leaves of the Lady's Mantle (*Alchemilla mollis*). The leaf of the Lady's Mantle is covered with stiff hairs which are hydrophilic by nature, whereas the leaf surface (the cuticula) is hydrophobic. Generally, one expects the leaf to be more hydrophilic due to the stiff hydrophilic hairs, but surprisingly, the leaf exhibits hydrophobicity. It is interesting to note the difference in the

wetting mechanism of the pPFDA-coated brush and the leaf of the Lady's Mantle. The leaf is hydrophobic, but not always. The wetting of the leaf depends on the pinning of the droplet to the hydrophilic hair,[52] whereas the wetting of the pPFDA-coated brush (or CNTs) depends on the low-energy (weak-pinning) pPFDA coating and roughness and is always hydrophobic.

■ CONCLUSION

An ultrathin, conformal, and low-surface-energy pPFDA coating was deposited on CNT micropillars via iCVD. The pPFDA-coated CNT pillars were tested for liquid stability, hydrophobicity, and omniphobicity. SEM and confocal-microscopy images confirmed that the pPFDA coating reinforced the individual CNTs and also introduced lateral welds between the individual, aligned CNTs, which made them robust to liquid infiltration and consequent drying, thereby preventing elastocapillary densification within the CNT micropillars. The pPFDA-coated CNT micropillars show better hydrophobicity and omniphobicity than the uncoated CNT micropillars because of the combined effects of the low-surface-energy pPFDA coating and the presence of re-entrant features on top of the pPFDA-coated CNT micropillars. Droplets of water, hexadecanethiol, acetone, dimethoxyethane, and ethylene glycol exhibited a stable Cassie–Baxter state on the pPFDA-coated CNT pillars. It was also demonstrated how to tune the wettability of these surfaces by plasma etching. The outcome of this study provides a stable and versatile method to control the wettability of porous microstructures for energy storage applications and for the microcontact printing of electronic features.

■ MATERIALS AND METHODS

Synthesis of Vertically Aligned Carbon Nanotubes. The patterned CNTs are initially grown by thermal CVD in a quartz-tube furnace (Thermo Fisher Minimite, 22 mm inner diameter). The catalyst for CNT growth is patterned on a (100) silicon wafer with 300 nm of thermally grown silicon dioxide by lift-off processing using photolithography, followed by ultrasonic agitation in acetone. The catalyst layer, 10 nm of Al_2O_3 and 1 nm of Fe, are sequentially deposited by electron-beam physical vapor deposition. The wafer with the deposited catalyst is diced into ∼2 × 2 cm pieces and placed in the quartz-tube furnace for CNT growth. The growth recipe starts with flowing 100/400 sccm of He/H_2 while heating the furnace up to 775 °C over 10 min (ramping step) and then holding it at 775 °C for 10 min with the same gas flow rates (annealing step). Then, for CNT growth, the gas flow is changed to 100/400/100 sccm of $C_2H_4/He/H_2$ at 775 °C for the selected duration. The typical growth rate is ∼100 μm/min. After the growth, the furnace is cooled down to <100 °C with the same gas flow and finally purged with 1000 sccm of He for 5 min.

iCVD Polymerization. A custom-built cylindrical reactor (diameter of 24.6 cm and height of 3.8 cm) is used to perform iCVD polymerization. An array of 14 parallel chromalloy filaments (Goodfellow) held around 2 cm above the reactor stage, where the growth substrates are kept, is used to heat the initiator (*tert*-butyl peroxide, TBPO, 98%, Aldrich) during polymerization. A quartz top (2.5 cm thick) covers the reactor, allowing real-time thickness monitoring via reflecting a 633 nm He−Ne-laser source (JDS Uniphase) off the substrate and polymer and recording the interference-signal intensity as a function of time. A mechanical Fomblin pump (Leybold, Trivac) is used to lower the pressure inside the reactor, and an MKS capacitive gauge is used to monitor the pressure. 1*H*,1*H*,2*H*,2*H*-perfluorodecyl acrylate (PFDA, 97%) and the TBPO (98%) initiator are used as received from Sigma-Aldrich. A mass-flow controller (1479 MFC, MKS Instruments) is used to adjust and deliver the TBPO at a constant flow rate of 1 sccm. A DC power

supply (Sorensen) is utilized to heat the filament to the desired temperature (T_f = 250 °C). At this filament temperature, the labile peroxide bond of the TBPO breaks and creates −TBO radicals. The PFDA monomer is vaporized inside a glass jar through heating of the jar to a temperature of 80 °C, and it is then introduced to the reactor in the vapor phase through a needle valve at a constant flow rate of 0.2 sccm. The temperature of the growth substrate is maintained at T_s = 30 °C during polymerization using a recirculating chiller and heater (NESLAB RTE-7). K-type thermocouples (Omega Engineering) are used for measuring all of the temperatures. A throttle valve (MKS Instruments) is used to maintain a pressure of 60 mTorr during the polymerization. A silicon wafer is used as a control substrate during the PFDA polymerization; the thickness of the pPFDA deposited on the control silicon substrate is measured in real time using an interferometer with a deposition rate of 1 nm/min.

Contact-Angle Measurements. Liquid-contact angles are measured by depositing droplets of 5 μL on the substrates using a goniometer equipped with an automated dispenser (Model 500, ramé-hart). Each contact-angle value is averaged from measurements of ten discrete droplets distributed across the sample. The surface tension values of the liquids are measured by the pendant drop method. Measurements are performed rapidly (less than 10 s) to minimize the impact of air exposure on the liquid droplets. The surface-tension values are averaged from measurements of ten droplets of a given liquid. The surface tension of distilled water measured in air, 71.0 ± 1.0 mN/m, is used for confirming the accuracy of the tensiometry measurements.

Characterization. XPS data are acquired using a spectrophotometer (PHI 5000 VersaProbe II) with an Al Kα X-ray source. The survey-scan spectra are collected at BE of 200−800 eV with a step size of 1 eV, a pass energy of 187.8 eV, a TOA of 45°, and a spot size of 200 μm. For high resolution, the instrument is utilized in a high-power mode with a raster scan of 100 μm spots over a 1 mm line. The pass energy and step size the for high-resolution spectra are 24 and 0.1 eV, respectively. Each measurement is examined in several spots to ensure reproducibility. Multipack software is utilized for analysis of the collected spectra, in which 70% Gaussian, 30% Lorentzian curve fitting is performed. FTIR are performed on a Nicolet Nexus 870 ESP spectrometer in a normal transmission mode equipped with an MCT detector and KBr beamsplitter. Spectra are acquired over the range of 500 to 4000 cm^{-1} with a 4 cm^{-1} resolution for 256 scans.

Imaging. A scanning electron microscope equipped with an energy-dispersive X-ray spectrometer, SEM-EDX (JEOL 6010LA), is used for the imaging and verification of the fluorine-containing-polymer deposition. In situ imaging of liquids on the coated CNT pillars is obtained using a Zeiss EVO-55 ESEM. The chamber of the ESEM is maintained at a pressure of 1000 Pa.

Confocal-microscopy images and videos are acquired as z-section stacks (z step = 1.07 μm) using a Nikon A1r confocal microscope equipped with a 20× Plan ApoVC, an NA 0.75 objective, and four imaging lasers (405, 488, 562, and 647 nm). For the images, the maximum projection of the z-stack sections and individual z sections are individually exported as TIFF files. Prior to confocal imaging, the liquids are dyed with fluorescent dye (fluorescein sodium salt, F6377 Sigma-Aldrich, 1% wt).

ASSOCIATED CONTENT

Ⓢ Supporting Information

The Supporting Information is available free of charge on the ACS Publications website at DOI: 10.1021/acsami.7b13713.

Supporting Information List of Contents and Figures S1−S10: schematic, SEM-EDX mapping and EDX emission spectrum images, FTIR spectra, XPS spectra, SEM images, top-view SEM images, 3D confocal-microscopy images, confocal-microscopy images, contact angle vs pPFDA thickness, schematic and SEM images (PDF)

Videos S1−S5 (video descriptions are available in the Supporting Information List of Contents) (ZIP)

Videos S6−S10 (video descriptions are available in the Supporting Information List of Contents) (ZIP)

Videos S11−S14 (video descriptions are available in the Supporting Information List of Contents) (ZIP)

AUTHOR INFORMATION

Corresponding Authors

*E-mail: kkg@mit.edu (K.K.G.).

*E-mail: gareth@mit.edu (G.H.M.).

ORCID Ⓘ

Hossein Sojoudi: 0000-0002-5278-9088

Hangbo Zhao: 0000-0001-5229-4192

A. John Hart: 0000-0002-7372-3512

Gareth H. McKinley: 0000-0001-8323-2779

Karen K. Gleason: 0000-0001-6127-1056

Notes

The authors declare no competing financial interest.

REFERENCES

(1) Li, W. Z.; Xie, S. S.; Qian, L. X.; Chang, B. H.; Zou, B. S.; Zhou, W. Y.; Zhao, R. A.; Wang, G. Large-scale synthesis of aligned carbon nanotubes. *Science* **1996**, *274* (5293), 1701−1703.

(2) Chen, Q. D.; Dai, L. M. Three-dimensional micropatterns of well-aligned carbon nanotubes produced by photolithography. *J. Nanosci. Nanotechnol.* **2001**, *1* (1), 43−47.

(3) Hart, A. J.; Slocum, A. H. Rapid growth and flow-mediated nucleation of millimeter-scale aligned carbon nanotube structures from a thin-film catalyst. *J. Phys. Chem. B* **2006**, *110* (16), 8250−8257.

(4) De Volder, M. F. L.; Tawfick, S. H.; Baughman, R. H.; Hart, A. J. Carbon Nanotubes. *Science* **2013**, *339* (6119), 535−539.

(5) Hayamizu, Y.; Yamada, T.; Mizuno, K.; Davis, R. C.; Futaba, D. N.; Yumura, M.; Hata, K. Integrated three-dimensional micro-electromechanical devices from processable carbon nanotube wafers. *Nat. Nanotechnol.* **2008**, *3* (5), 289−294.

(6) Chen, X.; Wang, H.; Yi, H.; Wang, X.; Yan, X.; Guo, Z. Anthraquinone on Porous Carbon Nanotubes with Improved Supercapacitor Performance. *J. Phys. Chem. C* **2014**, *118* (16), 8262−8270.

(7) Chen, H.; Roy, A.; Baek, J.-B.; Zhu, L.; Qu, J.; Dai, L. Controlled growth and modification of vertically-aligned carbon nanotubes for multifunctional applications. *Mater. Sci. Eng., R* **2010**, *70* (3−6), 63−91.

(8) Futaba, D. N.; Miyake, K.; Murata, K.; Hayamizu, Y.; Yamada, T.; Sasaki, S.; Yumura, M.; Hata, K. Dual Porosity Single-Walled Carbon Nanotube Material. *Nano Lett.* **2009**, *9* (9), 3302−3307.

(9) Izadi-Najafabadi, A.; Yasuda, S.; Kobashi, K.; Yamada, T.; Futaba, D.; Hatori, H.; Yumura, M.; Iijima, S.; Hata, K. Extracting the Full

Potential of Single-Walled Carbon Nanotubes as Durable Super-capacitor Electrodes Operable at 4 V with High Power and Energy Density. *Adv. Mater.* **2010**, 22 (35), E235−E241.

(10) Lu, W.; Goering, A.; Qu, L.; Dai, L. Lithium-ion batteries based on vertically-aligned carbon nanotube electrodes and ionic liquid electrolytes. *Phys. Chem. Chem. Phys.* **2012**, 14 (35), 12099−12104.

(11) Futaba, D. N.; Hata, K.; Yamada, T.; Hiraoka, T.; Hayamizu, Y.; Kakudate, Y.; Tanaike, O.; Hatori, H.; Yumura, M.; Iijima, S. Shape-engineerable and highly densely packed single-walled carbon nanotubes and their application as super-capacitor electrodes. *Nat. Mater.* **2006**, 5 (12), 987−994.

(12) Lau, K. K. S.; Bico, J.; Teo, K. B. K.; Chhowalla, M.; Amaratunga, G. A. J.; Milne, W. I.; McKinley, G. H.; Gleason, K. K. Superhydrophobic carbon nanotube forests. *Nano Lett.* **2003**, 3 (12), 1701−1705.

(13) Zhao, X.-M.; Wilbur, J. L.; Whitesides, G. M. Using Two-Stage Chemical Amplification To Determine the Density of Defects in Self-Assembled Monolayers of Alkanethiolates on Gold. *Langmuir* **1996**, 12 (13), 3257−3264.

(14) Chandra, D.; Yang, S. Stability of High-Aspect-Ratio Micropillar Arrays against Adhesive and Capillary Forces. *Acc. Chem. Res.* **2010**, 43 (8), 1080−1091.

(15) Bico, J.; Roman, B.; Moulin, L.; Boudaoud, A. Elastocapillary coalescence in wet hair. *Nature* **2004**, 432, 690−690.

(16) Kim, H.; Mahadevan, L. Capillary Rise between Elastic Sheets. *J. Fluid Mech.* **2006**, 548, 141−150.

(17) De Volder, M.; Hart, A. J. Engineering Hierarchical Nanostructures by Elastocapillary Self-Assembly. *Angew. Chem., Int. Ed.* **2013**, 52 (9), 2412−2425.

(18) De Volder, M.; Tawfick, S. H.; Park, S. J.; Copic, D.; Zhao, Z.; Lu, W.; Hart, A. J. Diverse 3D Microarchitectures Made by Capillary Forming of Carbon Nanotubes. *Adv. Mater.* **2010**, 22 (39), 4384−4389.

(19) De Volder, M. F. L.; Park, S. J.; Tawfick, S. H.; Vidaud, D. O.; Hart, A. J. Fabrication and electrical integration of robust carbon nanotube micropillars by self-directed elastocapillary densification. *J. Micromech. Microeng.* **2011**, 21 (4), 045033.

(20) Park, S. J.; Schmidt, A. J.; Tawfick, S. H.; Hart, A. J. Precise control of elastocapillary densification of nanostructures via low-pressure condensation. *J. Micromech. Microeng.* **2014**, 24 (6), 065019.

(21) Cassie, A. B. D.; Baxter, S. Wettability of porous surfaces. *Trans. Faraday Soc.* **1944**, 40, 546−551.

(22) Reeja-Jayan, B.; Kovacik, P.; Yang, R.; Sojoudi, H.; Ugur, A.; Kim, D. H.; Petruczok, C. D.; Wang, X.; Liu, A.; Gleason, K. K. A Route Towards Sustainability Through Engineered Polymeric Interfaces. *Adv. Mater. Interfaces* **2014**, 1 (4), 1400117.

(23) Sojoudi, H.; McKinley, G. H.; Gleason, K. K. Linker-free grafting of fluorinated polymeric cross-linked network bilayers for durable reduction of ice adhesion. *Mater. Horiz.* **2015**, 2 (1), 91−99.

(24) Sojoudi, H.; Walsh, M. R.; Gleason, K. K.; McKinley, G. H. Investigation into the Formation and Adhesion of Cyclopentane Hydrates on Mechanically Robust Vapor-Deposited Polymeric Coatings. *Langmuir* **2015**, 31 (22), 6186−6196.

(25) Gupta, M.; Gleason, K. K. Initiated Chemical Vapor Deposition of Poly(1H,1H,2H,2H-perfluorodecyl Acrylate) Thin Films. *Langmuir* **2006**, 22 (24), 10047−10052.

(26) Rivadulla, F.; Mateo-Mateo, C.; Correa-Duarte, M. A. Layer-by-Layer Polymer Coating of Carbon Nanotubes: Tuning of Electrical Conductivity in Random Networks. *J. Am. Chem. Soc.* **2010**, 132 (11), 3751−3755.

(27) He, P.; Shi, D. L.; Lian, J.; Wang, L. M.; Ewing, R. C.; van Ooij, W.; Li, W. Z.; Ren, Z. F. Plasma deposition of thin carbonfluorine films on aligned carbon nanotube. *Appl. Phys. Lett.* **2005**, 86 (4), 043107.

(28) Karaman, M.; Cabuk, N.; Ozyurt, D.; Koysuren, O. Self-supporting superhydrophobic thin polymer sheets that mimic the nature's petal effect. *Appl. Surf. Sci.* **2012**, 259, 542−546.

(29) Ye, Y.; Mao, Y.; Wang, F.; Lu, H.; Qu, L.; Dai, L. Solvent-free functionalization and transfer of aligned carbon nanotubes with vapor-deposited polymer nanocoatings. *J. Mater. Chem.* **2011**, 21 (3), 837−842.

(30) Journet, C.; Moulinet, S.; Ybert, C.; Purcell, S. T.; Bocquet, L. Contact angle measurements on superhydrophobic carbon nanotube forests: Effect of fluid pressure. *EPL (Europhysics Letters)* **2005**, 71 (1), 104.

(31) Wang, Z.; Ou, Y.; Lu, T.-M.; Koratkar, N. Wetting and Electrowetting Properties of Carbon Nanotube Templated Parylene Films. *J. Phys. Chem. B* **2007**, 111 (17), 4296−4299.

(32) Zhang, L.; Li, Z.; Tan, Y.; Lolli, G.; Sakulchaicharoen, N.; Requejo, F. G.; Mun, B. S.; Resasco, D. E. Influence of a top crust of entangled nanotubes on the structure of vertically aligned forests of single-walled carbon nanotubes. *Chem. Mater.* **2006**, 18 (23), 5624−5629.

(33) Kim, S.; Sojoudi, H.; Zhao, H.; Mariappan, D.; McKinley, G. H.; Gleason, K.; Hart, A. J. Ultrathin high-resolution flexographic printing using nanoporous stamps. *Science Advances* **2016**, 2 (12), e1601660.

(34) Tawfick, S.; Zhao, Z. Z.; Maschmann, M.; Brieland-Shoultz, A.; De Volder, M.; Baur, J. W.; Lu, W.; Hart, A. J. Mechanics of Capillary Forming of Aligned Carbon Nanotube Assemblies. *Langmuir* **2013**, 29 (17), 5190−5198.

(35) Chen, B.; Seidel, S.; Hori, H.; Gupta, M. Self-Assembly of Pillars Modified with Vapor Deposited Polymer Coatings. *ACS Appl. Mater. Interfaces* **2011**, 3 (11), 4201−4205.

(36) Chen, B.; Riche, C. T.; Lehmann, M.; Gupta, M. Responsive Polymer Welds via Solution Casting for Stabilized Self-Assembly. *ACS Appl. Mater. Interfaces* **2012**, 4 (12), 6911−6915.

(37) Matsunaga, M.; Aizenberg, M.; Aizenberg, J. Controlling the Stability and Reversibility of Micropillar Assembly by Surface Chemistry. *J. Am. Chem. Soc.* **2011**, 133 (14), 5545−5553.

(38) Tuteja, A.; Choi, W.; Ma, M.; Mabry, J. M.; Mazzella, S. A.; Rutledge, G. C.; McKinley, G. H.; Cohen, R. E. Designing Superoleophobic Surfaces. *Science* **2007**, 318 (5856), 1618−1622.

(39) Tuteja, A.; Choi, W.; Mabry, J. M.; McKinley, G. H.; Cohen, R. E. Robust Omniphobic Surfaces. *Proc. Natl. Acad. Sci. U. S. A.* **2008**, 105 (47), 18200−18205.

(40) De Volder, M. F. L.; Tawfick, S.; Park, S. J.; Hart, A. J. Corrugated Carbon Nanotube Microstructures with Geometrically Tunable Compliance. *ACS Nano* **2011**, 5 (9), 7310−7317.

(41) Paxson, A. T.; Varanasi, K. K. Self-similarity of contact line depinning from textured surfaces. *Nat. Commun.* **2013**, 4, 1492.

(42) Lobo, A. O.; Ramos, S. C.; Antunes, E. F.; Marciano, F. R.; Trava-Airoldi, V. J.; Corat, E. J. Fast functionalization of vertically aligned multiwalled carbon nanotubes using oxygen plasma. *Mater. Lett.* **2012**, 70, 89−93.

(43) Sun, Z.; Liu, Z.; Han, B.; Miao, S.; Miao, Z.; An, G. Decoration carbon nanotubes with Pd and Ru nanocrystals via an inorganic reaction route in supercritical carbon dioxide-methanol solution. *J. Colloid Interface Sci.* **2006**, 304 (2), 323−328.

(44) Van Hooijdonk, E.; Bittencourt, C.; Snyders, R.; Colomer, J.-F. Functionalization of vertically aligned carbon nanotubes. *Beilstein J. Nanotechnol.* **2013**, 4, 129−152.

(45) Ramos, S. C.; Vasconcelos, G.; Antunes, E. F.; Lobo, A. O.; Trava-Airoldi, V. J.; Corat, E. J. Wettability control on vertically-aligned multi-walled carbon nanotube surfaces with oxygen pulsed DC plasma and CO2 laser treatments. *Diamond Relat. Mater.* **2010**, 19 (7−9), 752−755.

(46) Ruelle, B.; Bittencourt, C.; Dubois, P. Surface treatment of carbon nanotubes via plasma technology. In *Polymer−Carbon Nanotube Composites*; McNally, T., Pötschke, P., Eds.; Woodhead Publishing: Cambridge, 2011.

(47) Majumder, M.; Chopra, N.; Hinds, B. J. Effect of tip functionalization on transport through vertically oriented carbon nanotube membranes. *J. Am. Chem. Soc.* **2005**, 127 (25), 9062−9070.

(48) De Volder, M. F. L.; Park, S. J.; Tawfick, S.; Vidaud, O. D.; Hart, A. J. Fabrication and electrical integration of robust carbon nanotube micropillars by self-directed elastocapillary densification. *J. Micromech. Microeng.* **2011**, 21, 045033.

(49) Srinivasan, S.; Chhatre, S. S.; Guardado, J. O.; Park, K.-C.; Parker, A. R.; Rubner, M. F.; McKinley, G. H.; Cohen, R. E. Quantification of feather structure, wettability and resistance to liquid penetration. *J. R. Soc., Interface* **2014**, *11* (96), 20140287.

(50) Autumn, K.; Liang, Y. A.; Hsieh, S. T.; Zesch, W.; Chan, W. P.; Kenny, T. W.; Fearing, R.; Full, R. J. Adhesive force of a single gecko foot-hair. *Nature* **2000**, *405* (6787), 681−685.

(51) Stark, A. Y.; Sullivan, T. W.; Niewiarowski, P. H. The effect of surface water and wetting on gecko adhesion. *J. Exp. Biol.* **2012**, *215* (17), 3080−3086.

(52) Bernardino, N. R.; Blickle, V.; Dietrich, S. Wetting of Surfaces Covered by Elastic Hairs. *Langmuir* **2010**, *26* (10), 7233−7241.